



## OPEN Establishing an end-to-end workflow for SNSPD fabrication and characterization

Shuyu Dong<sup>1,2</sup>, Darren Ming Zhi Koh<sup>3</sup>, Filippo Martinelli<sup>2,4</sup>, Pierre J. E. Brosseau<sup>2,4,5</sup>, Milos Petrovic<sup>2,7</sup>, Lijiong Shen<sup>3,8</sup>, Giorgio Adamo<sup>2,4</sup>, Anton N. Vetlugin<sup>2,4</sup>, Mariia Sidorova<sup>2,4,9</sup>, Christian Kurtsiefer<sup>3,6</sup> & Cesare Soci<sup>1,2,4</sup>✉

The outstanding performance of superconducting nanowire single-photon detectors (SNSPDs) has expanded their application areas from quantum technologies to astronomy, space communication, imaging, and LiDAR. As a result, there has been a surge in demand for these devices, that commercial products cannot readily meet. Consequently, more research and development efforts are being directed towards establishing in-house SNSPD manufacturing, leveraging existing nano-fabrication capabilities that can be customized and fine-tuned for specific needs. We report on the implementation of an end-to-end workflow for SNSPD fabrication and characterization, from superconducting film growth to meander nanowire fabrication and their integration with electrical readout circuits and optical testbeds. An essential aspect of this research involved identifying the key parameters of our workflow and developing reliable procedures for their optimization. As an outcome, the ab initio development of SNSPD technology yielded devices with characteristics comparable to commercial devices at a wavelength of 1550 nm, making them well-suited for telecommunication and integrated quantum systems. This report aims to provide useful insights to those entering the field and accelerate the establishment of superconducting detector technology and its application across various domains.

Superconducting nanowire single-photon detectors (SNSPDs) have become a state-of-the-art technology of quantum light detection with operation across visible, near- and middle-infrared spectral regions<sup>1</sup>. Their outstanding figures of merit, including close-to-unity detection efficiency<sup>2,3</sup>, gigahertz detection rate<sup>4</sup>, and sub-3 ps timing resolution (jitter)<sup>5</sup>, were demonstrated using different materials, designs and platforms. Not surprisingly, quantum technologies, such as quantum computing<sup>6,7</sup>, quantum key distribution (QKD)<sup>8,9</sup>, and quantum communication<sup>10</sup> eventually rely on these detectors. In addition, the high sensitivity and temporal performance of SNSPDs are extremely valuable for detecting weak classical light, for example, in deep-space communication<sup>11</sup>, neuromorphic computing<sup>12</sup>, and light detection and ranging (LiDAR) technologies<sup>13</sup>.

The swift expansion of SNSPDs across diverse application areas has significantly increased the demand for these devices and the need to establish in-house workflows for fabricating and characterizing SNSPDs<sup>14</sup>. This not only addresses the limited availability of commercial products, but also provides the flexibility to optimize detectors for specific needs. Importantly, establishment of SNSPD technology can leverage on nano-fabrication infrastructure commonly available in research institutions, enabling their cost-effective and rapid implementation.

Unfortunately, the workflow complexity and the sparsity of information available in the literature hinder straightforward establishment of SNSPD technology. Indeed, this technology involves development and optimization of various fabrication steps, including superconducting film deposition, nanofabrication, as well as integration of electrical readout circuits and implementation of light delivery strategies, which must be

<sup>1</sup>School of Electrical and Electronic Engineering, Nanyang Technological University, 639798 Singapore, Singapore.

<sup>2</sup>Centre for Disruptive Photonic Technologies, TPI, Nanyang Technological University, 637371 Singapore, Singapore.

<sup>3</sup>Centre for Quantum Technologies, National University of Singapore, 117543 Singapore, Singapore. <sup>4</sup>Division of Physics and Applied Physics, School of Physical and Mathematical Sciences, Nanyang Technological University, 637371 Singapore, Singapore. <sup>5</sup>Interdisciplinary Graduate Programme, Nanyang Technological University, 637460 Singapore, Singapore. <sup>6</sup>Department of Physics, National University of Singapore, 119077 Singapore, Singapore.

<sup>7</sup>Present address: Micron Semiconductor Asia Operations, 1 N Coast Dr, 757432 Singapore, Singapore. <sup>8</sup>Present address: School of Physics, Hangzhou Normal University, Zhejiang 311121, Hangzhou, China. <sup>9</sup>Present address: German Aerospace Center (DLR), Institute of Optical Sensor Systems, Rutherfordstr. 2, 12489 Berlin, Germany.

✉email: CSOCI@ntu.edu.sg

compatible with operation at cryogenic temperatures. While sufficient information is available on each of these aspects separately, there is limited literature on the implementation of all these tasks at system level.

Here we report the implementation of an end-to-end workflow for the fabrication and characterization of SNSPD devices. We provide detailed, step-by-step guidelines for all the critical fabrication processes, starting with superconducting film and ending with SNSPD device characterization in a cryostat. An essential aspect of our research involved identification of key workflow parameters and development of reliable procedures for their optimization. By systematically addressing each workflow step, we created a robust and replicable SNSPD fabrication procedure that can be seamlessly adopted to realize working single photon detectors and enhance their performance.

As a result, we were able to demonstrate SNSPD devices with performance metrics comparable to commercial detectors at a wavelength of 1550 nm, including temporal performance (reset time of approximately 60 ns and timing jitter of 74 ps), dark count rate (sub-Hz at 90% of maximum efficiency and 20 kHz at maximum efficiency), and internal detection efficiency (~95%). These characteristics are well-suited to meet the requirements of both fundamental research and field applications, including quantum communication and QKD, or classical imaging and LiDAR.

## Results

The outstanding characteristics of SNSPDs stem from their unique detection mechanism. The hotspot model suggests that photon absorbed in a supercurrent-carrying nanowire generates a localized normal hotspot, which expands across the entire wire cross-section, triggering a measurable signal<sup>15,16</sup>. The capacity to generate a compact hotspot with high electron energy density, which is necessary for effective photon detection, is largely determined by the superconducting film crystallographic disorder and its chemical composition<sup>17</sup>. Therefore, we first implemented a sputtering-and-measurement cycle to optimize the film quality described in the "Superconducting film deposition" subsection below. After film deposition optimization, the film with optimal parameters was used for nano-patterning into meandered nanowires, fabrication of electrical contacts, and integration with electrical circuits. Implementation of these steps, together with detector characterization techniques, are described in the following "From superconducting films to SNSPD devices" subsection.

### Superconducting film deposition

Niobium titanium nitride (NbTiN) was chosen as a material platform for this work as it enables high detection efficiency and excellent temporal performance in a single device<sup>2</sup>. Additionally, NbTiN detectors operate at the highest critical temperature among low- $T_c$  materials<sup>18,19</sup>. Note, however, that a similar workflow could be adopted for SNSPDs based on different superconducting materials, such as niobium nitride, molybdenum silicide, and tungsten silicide.

The NbTiN films were deposited in a reactive magnetron sputtering system (AJA Orion 8 UHV) in a mixed atmosphere of  $N_2$  and Ar. Films were sputtered on commercial silicon substrates (Rough Valley Microdevices) capped by a 266 nm ( $\pm 5\%$ ) thick dry thermal silicon oxide ( $SiO_2$ ) layer, at room temperature. Two separate source targets with niobium (3-inch Nb target; purity 99.99%) and titanium (2-inch Ti target; purity 99.99%) were installed in the ultrahigh vacuum chamber operating at a base pressure of  $< 5 \times 10^{-9}$  Torr (Fig. 1a). During superconducting films deposition, the Nb target was controlled with a DC (direct-current) of 375 mA, while the Ti target was controlled using RF (radio-frequency) wattage mode, with an applied power of 240 W (the deposition rates for each target were initially calibrated independently). The choice between DC and RF magnetron sputtering depends on the target's conductivity. During deposition in nitrogen gas, NbN and TiN form on the target surface, affecting conductivity. NbN is highly conductive, allowing for DC sputtering of Nb, while TiN has low conductivity, requiring RF sputtering of Ti. With these parameters set, we adjusted the sputtering power to achieve a NbTiN deposition rate of  $\sim 0.5$  Å/s and ensure high film quality (optimal disorder level, low surface roughness, etc.). Additionally, the deposition rates of Nb and Ti were balanced to achieve a  $Nb_xTi_{1-x}N$  composition stoichiometry of  $x = 0.62$ , which is most suitable for SNSPDs<sup>20</sup>.

### Crystallographic structure and morphology

To ensure the correct crystallographic structure, representative films were studied by X-ray diffractometry (XRD, Rigaku SmartLab). The XRD spectra of deposited films displayed a prominent NbTiN (111) peak next to the characteristic silicic peaks (Fig. 1b), confirming the face-centered cubic crystal structure of NbTiN with lattice constant of  $4.3 \pm 0.1$  Å, consistent with previously published data<sup>21</sup>. From the XRD spectrum, we can estimate the NbTiN grain size  $D$  by means of the Scherrer Eq. <sup>22</sup>,  $D = \frac{K\lambda}{\beta \cos\theta}$ . By substituting the values of the Scherrer constant ( $K = 0.89$ ), the X-ray wavelength ( $\lambda = 1.5406$  Å), the full width at half maximum of the diffraction peak ( $\beta = 9.23$  mrad), and half of the diffraction angle ( $\theta = 0.31$  rad), we estimate the grain size to be around 15 nm.

Besides crystallographic characteristics, optimization of superconducting films requires fine control of ultrathin thicknesses. The deposition rate of NbTiN is directly affected by the  $N_2$  flow rate and the chamber working pressure, as these parameters control the efficiency of energy transfer to the target, the so-called bombardment energy<sup>23</sup>. X-ray reflectivity spectra (Bruker D8 Discover with a copper K-alpha X-ray source) were used to accurately determine film thicknesses and calibrate deposition rates (Fig. 1c). The Materials Research software LEPTOS fitted the XRR profile with the thickness, roughness, and density as fitting parameters. The layer model included a silicon substrate and silica spacer with a fixed thickness of 266 nm. The oxide layer of NbTiN was excluded from the model, as it is expected to be thin – of the order of 1 nm<sup>24</sup>. Following this calibration procedure, we ensured that the thickness of all subsequent films was  $7 \text{ nm} \pm 5\%$ .

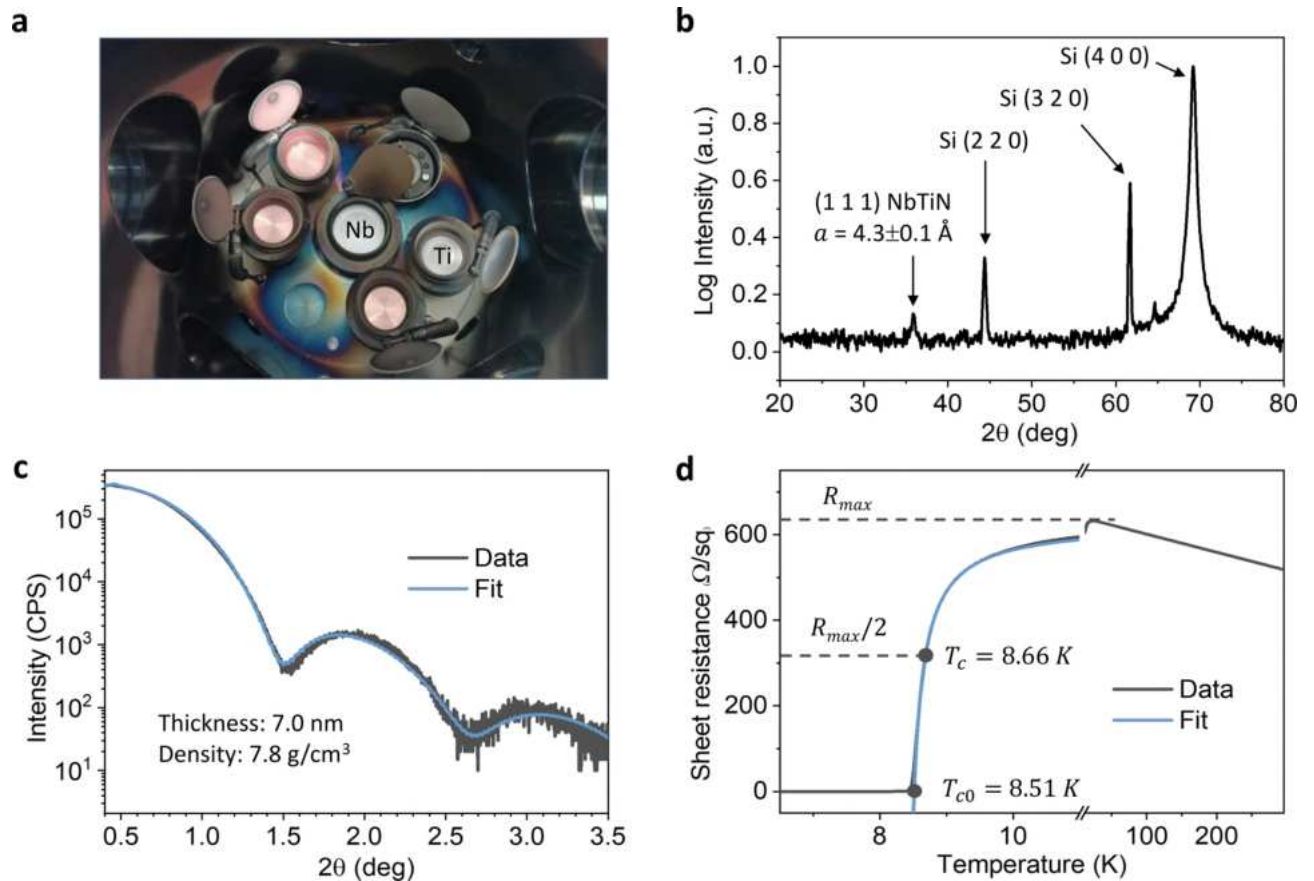


**Fig. 1.** Deposition-and-characterization cycle of superconducting films. (a) Material sources in the main sputtering chamber loaded with independent DC (direct-current) controlled Nb target and RF (radio-frequency) controlled Ti target. (b) Typical X-ray diffraction pattern of the deposited NbTiN films. (c) X-ray reflectivity spectrum (black line) of a representative NbTiN film. For the film in (c), the best-fit curve (blue line) yielded a thickness of 7.0 nm, mass density of  $7.8 \pm 0.2 \text{ g/cm}^3$ , and roughness of 0.1 nm. (d) The temperature-dependent sheet resistance of a representative NbTiN film obtained from DC transport measurements and used to determine its critical temperature. The film being measured was deposited at a working pressure of 2.5 mTorr with a  $\text{N}_2$  flow rate of 3.5 sccm and had a thickness of 7 nm.

Finally, to validate the quality of our films, we performed more reliable surface roughness measurements using an atomic force microscope (Cypher ES Environmental AFM). We found that the roughness of all films deposited under optimal or near-optimal conditions was below 1 nm with a typical value of 0.7 nm (0.2 nm in the XRR fitting), confirming their excellent morphological characteristics.

### Optimization of deposition parameters

$\text{N}_2$  flow rate and working pressure were identified as the most significant parameters to optimize film quality and SNSPD performance<sup>25,26</sup>. The  $\text{N}_2$  flow rate influences the stoichiometry and crystal structure of the film<sup>26,27</sup>, while the working pressure mainly affects the density of NbTiN polycrystalline grains<sup>25,28</sup>. To determine the optimal deposition parameters, we adjusted the  $\text{N}_2$  flow rate in the 1 to 4.5 sccm range (corresponding to an  $\text{N}_2$ -to-Ar ratio of 9% to 43%) and varied the working pressure in the 2 to 3 mTorr range<sup>20,29,30</sup>.

For each sputtered film, three critical characteristics, directly related to the performance of SNSPDs, were measured: transition temperature ( $T_c$ ), sheet resistance ( $R_{sq}$ ) at room temperature, and residual resistance ratio (RRR, the ratio of  $R_{sq}$  at 300 K to  $R_{sq}$  at 25 K). The  $T_c$  value is directly related to the superconducting gap energy, hence determining the detector's sensitivity to low-energy photons (the lower the  $T_c$ , the smaller the gap). The transition temperature of the film also sets an upper limit for the operating temperature of SNSPD devices, which is typically below  $0.5 T_c$ . The  $R_{sq}$  and RRR values, on the other hand, are related to the degree of disorder in the film, a decisive factor for confined hotspot formation and high photon detection efficiency<sup>31,32</sup>. Thin NbTiN films with thickness of  $d=7\text{--}9$  nm optimized for SNSPDs are expected to exhibit transition temperatures between 8.5 and 9.5 K, resistivity  $\rho = R_{sq}d$  between 320 and 380  $\mu\Omega \cdot \text{cm}$ , and RRR between 0.75 and 0.85 (see Refs. 20,33–35). These ranges serve us as the target for film optimization. The room-temperature sheet resistance and RRR were obtained from DC transport measurement, an example of which is shown in Fig. 1d. The transition temperature was estimated as the temperature at which the film resistance drops to half of its maximum value (8.66 K for the film in Fig. 1d). Due to the steepness of the superconducting phase transition, such estimate is

very close to the actual value (8.51 K in Fig. 1d), which can be rigorously obtained by fitting the data to the theory of 2D fluctuation conductivity (see Methods).

The results of the deposition-measurement optimization cycles are shown in Fig. 2. The room-temperature  $R_{sq}$  gradually grows with increasing  $N_2$  flow rate (Fig. 2a), which can be attributed to the increasing degree of disorder within the film. On the other hand, the transition temperature grows steadily with increasing flow rate until it reaches a maximum at 3.5 sccm (Fig. 2b). As depicted in Fig. 2c, this effect arises from the nitrogen tendency to occupy lattice vacancies, enhancing the stoichiometric balance of the film<sup>27</sup>. A further increase in the  $N_2$  flow rate tends to trigger a crystallographic phase transition in NbTiN, shifting from a face-centered cubic structure to a body-centered tetragonal structure. Correspondingly, the film becomes amorphous and the transition temperature degrades<sup>26</sup>.

Conversely, the working pressure regulates the density of NbTiN polycrystal grains<sup>25,28</sup>. As sketched in Fig. 2d, the grain density increases with working pressure. As a result, at higher working pressures the sheet resistance rises (Fig. 2a), since grain boundaries act as scattering centers in electron transport. At the same time, the transition temperature decreases (Fig. 2b), indicating the formation of a more homogeneously disordered granular system (refer to Chapter 8 in Ref. <sup>36</sup>).

This simple optimization cycle has allowed us to identify the best deposition regime for our superconducting films. As shown by yellow circles in Figs. 2a and 2b, the optimal  $N_2$  flow rate is 3.5 sccm and the optimal working pressure is 2.5 mTorr, as these conditions produced the optimal film that matched the targeted metrics. The optimal film, which was later used for SNSPD device fabrication, exhibited a high  $T_c$  of 8.7 K, relatively high  $R_{sq}$  of 518  $\Omega/sq$  ( $\rho = 363\mu\Omega \cdot cm$ ), and RRR of 0.83 (all films had RRR less than 1), is subsequently used for SNSPD device fabrication.

We note that for the films deposited at 2.5 and 3 mTorr, the sheet resistance differs more significantly than the critical temperature. Higher resistance indicates a greater level of disorder, which enhances hotspot confinement and, in turn, may improve detection efficiency. However, increased resistance may also lower the current density, resulting in a larger timing jitter. This trade-off can be addressed in future optimization steps depending on the specific performance requirements of the detector.

### From superconducting films to SNSPD devices

Optimized NbTiN thin films were patterned into a meandered nanowire structure (Fig. 3a) using two lithographic steps. First, photolithography (Karl Suss MJB4 Mask Aligner) was used to pattern electrodes using

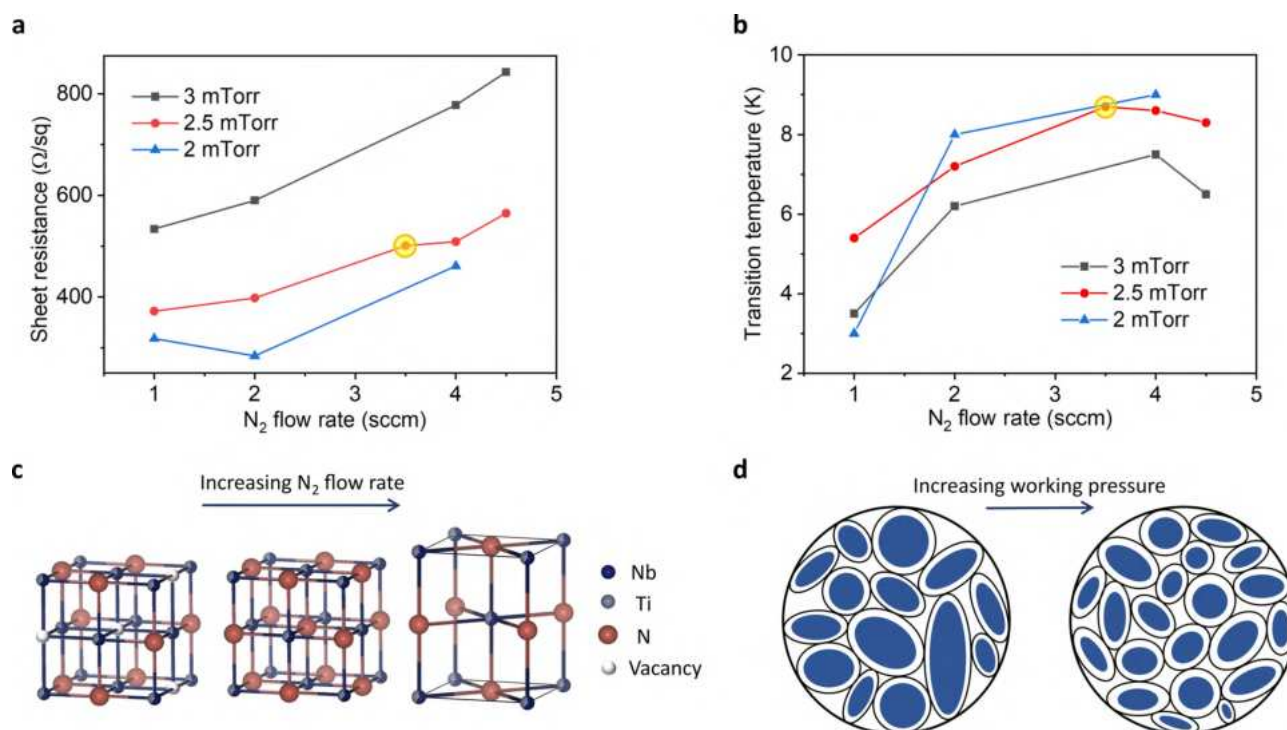


**Fig. 2.** Optimization of NbTiN film deposition parameters. (a) Room-temperature sheet resistance and (b) transition temperature for NbTiN films deposited at different working pressure and  $N_2$  flow rate. The optimal target values are highlighted by a yellow circle. (c) Schematic of the change of NbTiN crystal structure with increasing  $N_2$  flow rate: the structure on the left (lower  $N_2$  flow rate) is face-centered cubic with several vacancies; the structure in the middle (intermediate  $N_2$  flow rate) is face-centered cubic with fully filled vacancies; the structure on the right (higher  $N_2$  flow rate) is body-centered tetragonal<sup>26</sup>. (d) Schematic of the change of NbTiN granularity with increasing working pressure: grains and boundaries are represented by blue and white ovals, respectively.

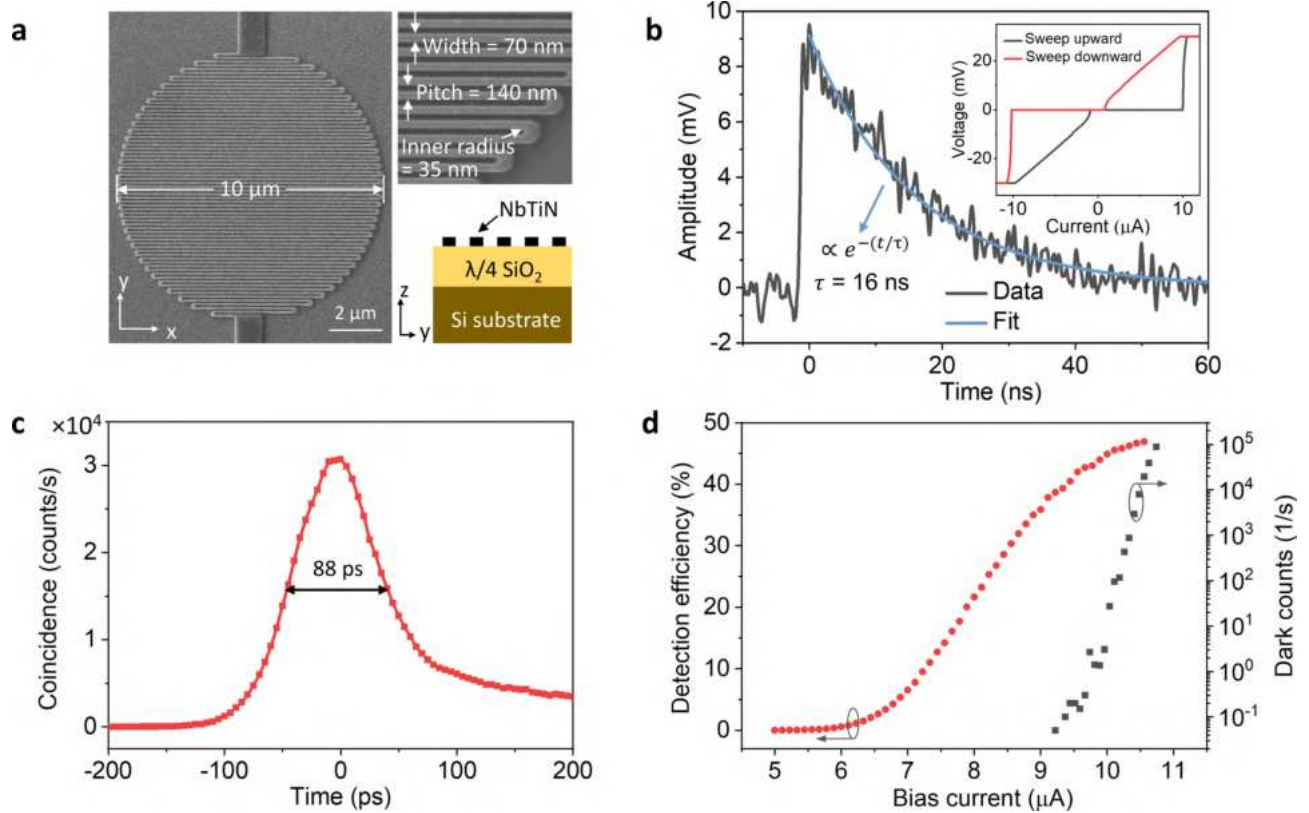


**Fig. 3.** Performance of the SNSPD device. (a) SEM image of the SNSPD. Upper inset: zoom-in SEM image. Lower inset: a sketch of the optical Salisbury-screen stack. (b) Output voltage pulse from the SNSPD amplified by one amplifier. Inset: current–voltage (I–V) measurement. (c) System timing jitter. (d) System detection efficiency and dark count rate.

AZ5214E photoresist, followed by Cr and Au thermal evaporation (HV-experimentation system UNIVEX 250). Then, the nanowire meander was patterned by electron beam lithography (FEI Helios Nanolab 650), using a low-temperature negative E-beam resist AR-N 7520.073 to prevent the peel off of the low adhesion NbTiN films. Finally, the superconducting nanowire was defined by reactive ion etching (RIE; Oxford PlasmaLab 80) in  $\text{CF}_4$ , maintaining an etch rate of approximately 0.1 nm/s to minimize the line edge roughness of the nanowire (see Methods).

A nanowire width of  $w = 70$  nm with a pitch of 140 nm (Fig. 3a) was chosen to achieve high photon sensitivity at 1550 nm and a high filling factor of 50% for enhanced light absorption. We used a circular bend design with inner and outer curvature radii of  $w/2$  and  $3w/2$  and a (ultimate) bend width of  $2w$  to reduce the current crowding effect, which occurs at the sharp nanowire bends, causing vortex nucleation and dark counts generation that limits the critical current, as shown in the upper inset of Fig. 3a. The circular geometry of the meander, with a 10  $\mu\text{m}$  diameter (Fig. 3a), ensures matching of the detector dimension with the typical telecom optical fibre core. The SNSPD optical stack was implemented in the Salisbury-screen type geometry (lower inset of Fig. 3a), where the absorbing nanowire was fabricated on top of a  $\lambda/4$ -spacer of silicon dioxide ( $266 \text{ nm} \pm 5\%$ ) on the silicon substrate. The  $\lambda/4$ -spacer ensures that the SNSPD is placed at the anti-node of the standing wave formed via interference of the incoming wave and wave reflected from the silicon substrate<sup>37</sup>. The electric field is maximum at the anti-node position, thus enhancing light absorption in the SNSPD. As discussed in the following, an ideal substrate should be fully reflective (e.g., covered by a metallic layer) to attain maximum absorption. On the other side, a standard thermal oxide silicon wafer significantly simplifies SNSPD fabrication, while providing relatively high absorption efficiency of  $(44 \pm 3)\%$ , when taking into account device layout, nanowire geometry, optical stack parameters, and their uncertainties<sup>37</sup>.

The fabricated SNSPDs were measured in a close-cycle cryostat (Entropy Cryogenics m-series) with a base temperature of 3.1 K. They were mounted on a copper holder and wire bonded to the contact pads of a custom-printed circuit board (PCB). The PCB with the detectors was placed on the cold plate of the cryostat. A single piece of a spliced single-mode fiber glued to the cryostat feed-through delivered light to the detectors. A tapered end of the fiber inside the cryostat was fixed on a nanopositioner (SmarAct XYZ-SLC) and coupled to the SNSPD at a distance of about 20  $\mu\text{m}$ , allowing efficient light delivery to the detector. The light polarization was adjusted with a polarization controller (Thorlabs FPC030) by maximizing the SNSPD count rate. The SNSPD performance was evaluated by measuring its critical current, reset time, timing jitter, dark count rate, and detection efficiency.

At first instance, the quality of the SNSPD fabrication can be assessed from the value of the critical current. At a base temperature of 3.1 K, we observed the transition to a normal state at a critical current of 10.6  $\mu\text{A}$ . The corresponding critical current density of 2.16 MA/cm<sup>2</sup> is approximately 60% of the theoretical limit of 3.61 MA/cm<sup>2</sup> estimated for a straight nanowire segment with the same geometry. The theoretical calculations were conducted on the base of the Ginzburg–Landau model<sup>38</sup> with a dirty-limit correction<sup>39</sup> and a diffusion coefficient of 0.48 cm<sup>2</sup>/s<sup>18</sup>. We note that the 60% level is close to the highest-reported values in nitride-based nanostructures ( $\approx 60\text{--}75\%$ )<sup>31,40</sup>, indicating high-quality nanofabrication.

The SNSPD response to input photons was studied by sending light through the optical fiber. A typical output voltage pulse of the SNSPD is shown in Fig. 3b. The pulse decay is governed by the exponential return of the bias current to the nanowire with kinetic inductance ( $L_k$ ) from the readout circuit with 50  $\Omega$  impedance. The decay time constant ( $\tau = L_k/50\Omega$ ) is obtained by fitting the pulse's falling edge with the exponential function  $\propto \exp(-t/\tau)$ . Thus determined time value ( $\tau \approx 16$  ns) results in the total device inductance of  $L_k = 800$  nH and a sheet kinetic inductance of approximately,  $L_k/[l/w] \approx 100$  pH/sq ( $l \approx 560\ \mu\text{m}$  is the total nanowire length), which is consistent with previous studies<sup>41</sup>. The detector's reset (dead) time refers to the duration required for the current to fully return to the nanowire or for the voltage to decay to the baseline noise level. In our SNSPD, this reset time is approximately 60 ns. The formation and collapse of a resistive domain within the nanowire, crucial for the self-reset mechanism, were also confirmed through the current–voltage (I–V) measurement. As shown in the inset in Fig. 3b, the SNSPD exhibits a typical hysteresis, with the switching current exceeding the return (hysteresis) current.

The timing jitter was measured via coincidence counts between the SNSPD and commercial silicon avalanche photodiode (Si-APD, PDM series of Micro Photon Devices) illuminated by correlated photon pairs (see Methods). The coincidence distribution depicted in Fig. 3c arises from the convolution of the response functions across the entire measurement system. The most significant contributions to the total distribution width ( $\sigma_{system}$ ) come from the SNSPD itself ( $\sigma_{SNSPD}$ ), the reference photodiode ( $\sigma_{APD}$ ) and the readout electronics ( $\sigma_{elec}$ ):  $\sigma_{system}^2 = \sigma_{SNSPD}^2 + \sigma_{APD}^2 + \sigma_{elec}^2$ . From the measured  $\sigma_{system} = 88$  ps, spec sheets values  $\sigma_{APD} = 35$  ps, and  $\sigma_{elec} = 34$  ps (see Methods), we estimate  $\sigma_{SNSPD}$  to be below 74 ps. We attribute the non-Gaussian tail observed in Fig. 3c to the Si-APD response function. In Ref. <sup>42</sup>, it was shown that the asymmetrical APD response is described by two Gaussian components, one of which is multiplied by the exponentially decaying function.

The system detection efficiency (SDE) was measured at a wavelength of 1550 nm by comparing count rates of the SNSPD and a reference detector with calibrated efficiency (InGaAs avalanche photodiode, ID Quantique, SDE = 10% at 1550 nm). To ensure measurement accuracy, both classical and quantum light sources were used for this measurement. The classical source – an attenuated CW laser at 1550 nm, is more accessible and easier to implement, while the quantum source – correlated photon pairs from spontaneous parametric down-conversion (SPDC), allows excluding two- and higher-order-photon contributions and dark counts which are unavoidable when measuring with the laser. For photon-pair illumination, the coincidence counts between the SNSPD/reference detector and the trigger detector (Si-APD) were compared. The SDE measurements with classical and quantum light sources differed by a few percent (see Methods), likely due to the different photon statistics of the two light sources and the intrinsic accuracy of the measurements. The maximum SDE,  $\eta_{max} = (47 \pm 2.5)\%$ , was recorded at the critical current (Fig. 3d). This value is in agreement with the absorption efficiency calculated for this device<sup>37</sup>, indicating that the detector's efficiency is close to saturation.

The dark count rate was measured by turning off the light source and recording the counts. Additionally, the tip of the optical fiber was moved away from the detector's sensitive area to diminish the absorption of blackbody radiation propagating through the fiber. The dark count rate, shown with gray squares in Fig. 3d, remains at the sub-Hz level for SDE less than  $0.9\eta_{max}$ , after which it grows exponentially reaching 20 kHz at  $\eta_{max}$ .

## Discussion

We provided a comprehensive account of the development of an end-to-end workflow for fabrication and optimization of SNSPD devices in our laboratories. The initial crucial stage was to establish deposition of high-quality superconducting films by magnetron sputtering. We have identified the N<sub>2</sub> flow rate and the working pressure as the primary parameters affecting film quality and SNSPD performance, while other factors such as base pressure, power applied to the Nb and Ti targets, and argon flow rate, can be safely set to default values. Characterization and optimization of superconducting films relied on DC transport measurements conducted from room to cryogenic temperatures. Additionally, X-ray reflectivity measurements were necessary to calibrate thin film deposition rate, while X-ray diffraction and AFM measurements were useful to confirm crystallographic structure and morphological quality of the films. The subsequent critical step was establishing a reliable nanofabrication protocol. Fabrication quality requirements become more stringent for SNSPD operating in the mid-IR range, since constrictions in the wires or edge roughness limit the critical current and hence the spectral sensitivity. It is worth noting that although micro-wide wires have recently demonstrated saturated internal detection efficiency at wavelengths below 850 nm<sup>43</sup>, narrow nanowires exhibit better spectral performance and are preferred for mid-IR photon detection<sup>1</sup>.

Other workflow steps, including electrical contact fabrication, contact wire bonding to a dedicated PCB, and optical coupling, are straightforward and relatively easy to implement. Finally, SNSPD characterization required the establishment of DC and RF electrical measurements and photon counting techniques. While measurements based on correlated photon pairs from SPDC source are, in general, more accurate, characterizing SNSPDs with strongly attenuated classical light sources, such as pulsed lasers, also provide feasibility with minimal discrepancy from most accurate SPDC measurements.

Following this procedure, we realized SNSPD devices with characteristics comparable to commercial products<sup>44–46</sup>. Henceforth, optimization steps should be determined by the requirements of the specific

application. For instance, close-to-unity system detection efficiency would be required for quantum computing, and it can be achieved by adopting more sophisticated optical designs to increase light absorption. This could involve resonant structures based on highly reflective mirrors<sup>2</sup>, distributed Bragg reflectors<sup>47</sup>, or coherent absorption schemes<sup>37,48</sup>. Also, the internal efficiency could be improved by enhancing the current density using an optimal bend design with elliptical curvature (see Eq. (91) in Ref. 49), which eliminates current crowding but limits the filling factor to 33%. A novel L-shape bend design<sup>50</sup> as well as a sophisticated bend-thickening approach<sup>51</sup> solve both issues, eliminating the current crowding and enabling high filling factor. For high-speed quantum communication and QKD, faster detectors would be preferable, with shorter or customized nanowire designs such as parallel<sup>52</sup> and interleaved<sup>4</sup> configurations or distributed SNSPD arrays<sup>37</sup>. We note that the improvement of one parameter (e.g., temporal response) often requires sacrificing other figures of merit (e.g., efficiency), and the best tradeoff is defined by the specific application.

## Conclusions

In conclusion, we have systematically addressed the most critical steps needed for the realization of working SNSPD prototypes and their optimization. Our robust and reproducible workflow could be seamlessly adopted in other research laboratories to facilitate the establishment of in-house SNSPD technology. The ability to fine-tune and configure SNSPD devices on demand holds great potential to expedite further development of SNSPD technology and its wide range of fundamental and practical applications.

## Methods

### SNSPD fabrication

The nanowire meander was patterned by electron beam lithography (FEI Helios Nanolab 650), using a low-temperature negative E-beam resist AR-N 7520.073. The resist was spin-coated at 4000 rpm for 60 s, resulting in a 100 nm thick layer. The sample was then baked at 85 °C for 2 min. The optimal area dose for e-beam lithography ranges from 260 to 300  $\mu\text{C}/\text{cm}^2$ , using a beam energy of 30 kV and a beam current of 13 pA. After e-beam exposure, the sample was developed for 90 s in a solution of AR-N 300–47 and deionized water mixed in a 4:1 volume ratio. The development was stopped by immersing the sample in deionized water for 30 s. Finally, the nanowire structure was etched using reactive ion etching (Oxford PlasmaLab 80) with  $\text{CF}_4$  gas flowing at the rate of 50 sccm. The etching process was conducted at the power of 80 W for 80 s for a 7 nm-thick NbTiN film.

### Cryogenic measurements of superconducting films and SNSPDs

Unpatterned films were measured in a close-cycle cryostat with base temperature of 3.7 K (DRY ICE 3 K). The room-temperature sheet resistance  $R_{sq}$  was directly measured with ST2253 Digital Four Probe Tester, with the van der Pauw method<sup>53</sup>. For resistance measurements at lower temperatures, a two-probe method was used by bonding the film to a PCB using a wire-bonder (West bond 7476E-79) and connecting it to DC lines inside the cryostat. Here, the resistance was determined by applying a current of 100  $\mu\text{A}$  with a DC source (Yokogawa GS200) and measuring the voltage (BK Precision 5492C). The sheet resistance at other temperatures (plotted in Fig. 1d) was then calculated using the ratio of  $R_{sq}$  to the directly measured resistance at room temperature.

The transition temperature is rigorously determined by fitting the experimental  $R_{sq}(T)$  data in Fig. 1d using the expression provided by the theory of 2D fluctuation conductivity<sup>54,55</sup>  $R_{sq}(T) = \left[ \frac{1}{R_{SN}} + A_{2d} \frac{1}{16} \frac{e^2}{\hbar \ln(T/T_{C0})} \right]^{-1}$

, which is valid for  $\ln(T/T_C) \ll 1$ , i.e., when the temperature approaches the transition temperature  $T_C$  from the right and  $\approx 1.1T_C$  from the left. Here  $\hbar$  is the reduced Planck constant,  $e$  is the elementary charge,  $A_{2d}$  and  $R_{SN}$  are the fitting parameters of about unity and the maximum  $R_{sq}(T)$  value, respectively. For the data shown in Fig. 1d, the best fit yielded  $T_C = 8.51\text{K}$ .

SNSPD devices were measured in a close-cycle cryostat with base temperature of 3.1 K (the Entropy Cryogenics m-series). They were biased with a Rohde & Schwarz Hmc8042 voltage source in series with a 270 k  $\Omega$  resistor through a room-temperature bias-T (Minicircuits ZB85-12G-S+). The signal from the SNSPD was amplified with a low-noise room-temperature amplifier (Minicircuits ZFL-1000LN+) with nominal bandwidth of 0.1–1000 MHz. The amplified SNSPD pulses were recorded with an oscilloscope (Lecroy waverunner 8404 M) and counted with a time-to-digital converter (TDC1 by S-Fifteen Instruments).

A noise jitter of 34 ps was determined as the ratio of the FWHM noise level (18.2 mV) in the baseline of a recorded voltage pulse to the 20–80% slope of its rising edge (0.54 mV/ps). Jitter contributions by the time-tagger (scope) and the photon pair source<sup>56</sup> were below 2 ps and 1 ps, respectively.

### Single-photon system detection efficiency

The SNSPD detection efficiency was measured using a reference calibrated detector and either classical or quantum light sources<sup>57</sup>.

### Measurement with attenuated laser

Here (Fig. 4a), we used an attenuated continuous wave (CW) 1550 nm laser (MLD-D55S2-2A10P8). The laser intensity was attenuated with fixed fiber attenuators (Thorlabs) so that the SNSPD photon count rate was kept below several thousand counts per second to ensure a linear regime well below the maximum count rate of approximately 16 MHz (inverse reset time 1/60 ns). The system detection efficiency ( $\eta_{\text{SNSPD}}$ ) was estimated

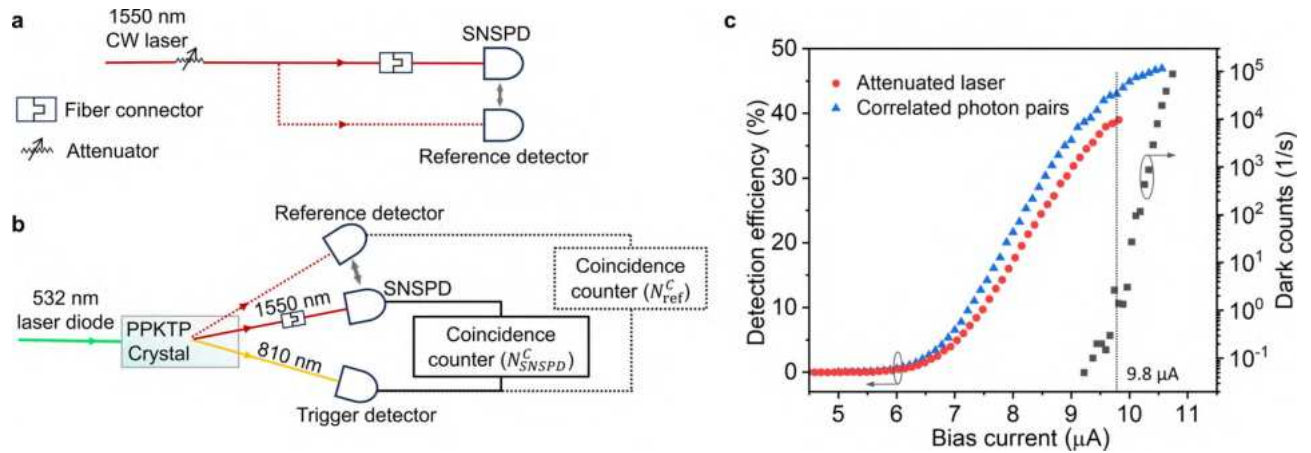


**Fig. 4.** Schematics of the two methods used for SDE calibration with (a) a classical attenuated coherent light source and (b) a quantum correlated-photon-pair source. (c) System detection efficiency and dark count rate obtained with the two different methods as a function of SNSPD biasing current; the dash line indicates the 9.8  $\mu\text{A}$  bias current at which the device performance was assessed.

comparing the SNSPD count rate ( $N_{\text{SNSPD}}$ ) with the count rate ( $N_{\text{ref}}$ ) of the reference detector (InGaAs avalanche photodiode; ID Quantique ID Qube) under equal photon flux:

$$\eta_{\text{SNSPD}} = \eta_{\text{ref}} \frac{N_{\text{SNSPD}}}{N_{\text{ref}}} \frac{1}{\eta_f},$$

where the system detection efficiency of the reference detector,  $\eta_{\text{ref}} = (10 \pm 0.5)\%$ , was independently calibrated by the manufacturer. We also account for the loss due to the finite transmission ( $\eta_f = 0.6$ ) of the spliced fiber used to deliver light to the SNSPD. The SNSPD system detection efficiency measured with the attenuated laser is shown by the red circles in Fig. 4c.

### Measurement with correlated photon pairs

In this experiment (Fig. 4b), we replaced the attenuated laser with the source of correlated photon pairs. The photon pairs were generated via SPDC in a periodically poled potassium titanyl phosphate (PPKTP) crystal pumped by a 532 nm laser diode (Thorlabs DJ532-40). In the non-degenerate SPDC, each photon pair consisted of one photon at a wavelength of 1550 nm and one photon at a wavelength of 810 nm. The 1550 nm photons were directed to either SNSPD or the reference detector (InGaAs avalanche photodiode), while the 810 nm photons were sent to a trigger detector (Si-APD, Micro Photon Devices, PDM series). We recorded the coincidence count rates between the SNSPD and the trigger detector ( $N_{\text{SNSPD}}^{\text{C}}$ ) and between the reference and trigger detectors ( $N_{\text{ref}}^{\text{C}}$ ) under equal illumination conditions. If  $N$  is the generation rate of the correlated photon pairs, the coincidence count rates can be expressed as

$$N_{\text{SNSPD}}^{\text{C}} = (\eta_{\text{SNSPD}} \eta_{\text{loss}} \eta_f) (\eta_{\text{trig}} \eta_{\text{loss,t}}) N,$$

$$N_{\text{ref}}^{\text{C}} = (\eta_{\text{ref}} \eta_{\text{loss}}) (\eta_{\text{trig}} \eta_{\text{loss,t}}) N,$$

where  $\eta_{\text{SNSPD}}$ ,  $\eta_{\text{ref}}$  and  $\eta_{\text{trig}}$  are system detection efficiencies of the SNSPD, reference and trigger detectors, respectively; and  $\eta_{\text{loss}}$  and  $\eta_{\text{loss,t}}$  represent the efficiencies of delivering 1550 nm and 810 nm photons from the PPKTP crystal to the corresponding detectors. As before, we also account for the transmission efficiency of the spliced fiber delivering light to the SNSPD, denoted as  $\eta_f$ . Thus, the SNSPD efficiency is given by:

$$\eta_{\text{SNSPD}} = \eta_{\text{ref}} \frac{N_{\text{SNSPD}}^{\text{C}}}{N_{\text{ref}}^{\text{C}}} \frac{1}{\eta_f},$$

The corresponding measurements are represented by the blue triangles in Fig. 4(c). There is a few percent difference in the SNSPD system detection efficiency measured using classical and quantum light sources. For example, at the bias current of 9.8  $\mu\text{A}$ , the efficiency measured with classical light is  $(39 \pm 2.5)\%$ , whereas with quantum light it is  $(44 \pm 2.5)\%$ . The difference in these estimates is nearly within the uncertainty bounds, while the difference in photon statistics of classical and quantum light sources may also play a role. The uncertainty of the efficiency is calculated using the error propagation formula, where the uncertainty of the reference detector contributes the most,  $\eta_{\text{ref}} = (10 \pm 0.5)\%$ .

## Light absorption in SNSPD

In calculating light absorption in the SNSPD, we followed Ref. 37 and replaced the ideal reflecting mirror (Fig. 2 in Ref. 37) with a silicon substrate. Specifically, we used a transfer matrix method to calculate the optical response of the optical stack. Input, spacer and output medium were described by refractive indices of 1 (air), 1.44 (silica) and 3.47 (silicon), respectively. The SNSPD was treated as a uniform layer with effective permittivity  $f\epsilon_{\text{NbTiN}} + (1-f)\epsilon_{\text{air}}$ , where  $\epsilon_{\text{NbTiN}} = 4.21 + i3.87$  and  $\epsilon_{\text{air}} = 1$  are the permittivity of NbTiN and air, and  $f$  is the filling factor. For SNSPD thickness of  $7 \pm 0.5$  nm, spacer thickness of  $\lambda/4 \pm 5\%$ , and filling factor of  $0.50 \pm 0.05$ , we evaluated the SNSPD absorption to be  $44 \pm 3\%$ .

## Data availability

The data that support the findings of this study are openly available in NTU research data repository DR-NTU (data) at <https://doi.org/10.21979/N9/VH0WLX>.

Received: 20 August 2024; Accepted: 27 November 2024

Published online: 28 December 2024

## References

- Taylor, G. G. et al. Low-noise single-photon counting superconducting nanowire detectors at infrared wavelengths up to 29  $\mu\text{m}$ . *Optica* **10**, 1672–1678 (2023).
- Chang, J. et al. Detecting telecom single photons with 99.5–2.07+0.5% system detection efficiency and high time resolution. *APL Photonics* **6**, 036114 (2021).
- Reddy, D. V., Nerem, R. R., Nam, S. W., Mirin, R. P. & Verma, V. B. Superconducting nanowire single-photon detectors with 98% system detection efficiency at 1550 nm. *Optica* **7**, 1649–1653 (2020).
- Resta, G. V. et al. Gigahertz detection rates and dynamic photon-number resolution with superconducting nanowire arrays. *Nano Lett.* **23**, 6018–6026 (2023).
- Korzth, B. et al. Demonstration of sub-3 ps temporal resolution with a superconducting nanowire single-photon detector. *Nat. Photon.* **14**, 250–255 (2020).
- Hampel, B. et al. Trap-integrated superconducting nanowire single-photon detectors with improved rf tolerance for trapped-ion qubit state readout. *Appl. Phys. Lett.* **122** (2023).
- Zhong, H.-S. et al. 12-photon entanglement and scalable scattershot boson sampling with optimal entangled-photon pairs from parametric down-conversion. *Phys. Rev. Lett.* **121**, 250505 (2018).
- Grünenfelder, F. et al. Fast single-photon detectors and real-time key distillation enable high secret-key-rate quantum key distribution systems. *Nat. Photon.* **17**, 422–426 (2023).
- Chen, J.-P. et al. Sending-or-not-sending with independent lasers: secure twin-field quantum key distribution over 509 km. *Phys. Rev. Lett.* **124**, 070501 (2020).
- Bhaskar, M. K. et al. Experimental demonstration of memory-enhanced quantum communication. *Nature* **580**, 60–64 (2020).
- Grein, M. et al. An optical receiver for the Lunar Laser Communication Demonstration based on photon-counting superconducting nanowires, Vol. 9492 CSI (SPIE, 2015).
- Shastri, B. J. et al. Photonics for artificial intelligence and neuromorphic computing. *Nat. Photon.* **15**, 102–114 (2021).
- Li, Z.-P. et al. Single-photon computational 3D imaging at 45 km. *Photon. Res.* **8**, 1532–1540 (2020).
- Alexander, K. et al. A manufacturable platform for photonic quantum computing. *arXiv preprint arXiv:2404.17570* (2024).
- Natarajan, C. M., Tanner, M. G. & Hadfield, R. H. Superconducting nanowire single-photon detectors: physics and applications. *Supercond. Sci. Technol.* **25**, 063001 (2012).
- Nicolich, K. L. et al. Universal model for the turn-on dynamics of superconducting nanowire single-photon detectors. *Phys. Rev. Appl.* **12**, 034020 (2019).
- Vodolazov, D. Y. Single-photon detection by a dirty current-carrying superconducting strip based on the kinetic-equation approach. *Phys. Rev. Appl.* **7**, 034014 (2017).
- Sidorova, M. et al. Magnetoconductance and photoresponse properties of disordered NbTiN films. *Phys. Rev. B* **104**, 184514 (2021).
- Ma, R. et al. Disorder enhanced relative intrinsic detection efficiency in NbTiN superconducting nanowire single photon detectors at high temperature. *Appl. Phys. Lett.* **124** (2024).
- Zichi, J. et al. Optimizing the stoichiometry of ultrathin NbTiN films for high-performance superconducting nanowire single-photon detectors. *Opt. Express* **27**, 26579–26587 (2019).
- Myoren, H., Shimizu, T., Iizuka, T. & Takada, S. Properties of NbTiN thin films prepared by reactive DC magnetron sputtering. *IEEE Trans. Appl. Supercond.* **11**, 3828–3831 (2001).
- Vinila, V. S. & Isac, J. in *Design, Fabrication, and Characterization of Multifunctional Nanomaterials* (eds Sabu Thomas, Nandakumar Kalarikkal, & Ann Rose Abraham) 319–341 (Elsevier, 2022).
- Maezawa, H., Sato, T. & Noguchi, T. Process simulation of reactive DC magnetron sputtering for thin film deposition of niobium-titanium nitride. *IEEE Trans. Appl. Supercond.* **15**, 3520–3523 (2005).
- Zhang, L., You, L., Ying, L., Peng, W. & Wang, Z. Characterization of surface oxidation layers on ultrathin NbTiN films. *Phys. C: Supercond. Appl.* **545**, 1–4 (2018).
- Cecil, T. W., Weikle, R. M., Kerr, A. R. & Lichtenberger, A. W. Investigation of NbTiN thin films and AlN tunnel barriers with ellipsometry for superconducting device applications. *IEEE Trans. Appl. Supercond.* **17**, 3525–3528 (2007).
- Yeram, S. S., Bhakat, S., Dash, S. S. & Pal, A. Structural transitions in superconducting NbTiN thin films. *arXiv preprint arXiv:2311.14154* (2023).
- Makise, K., Terai, H., Takeda, M., Uzawa, Y. & Wang, Z. Characterization of NbTiN Thin films deposited on various substrates. *IEEE Trans. Appl. Supercond.* **21**, 139–142 (2011).
- Iosad, N. N. et al. Optimization of RF- and DC-sputtered NbTiN films for integration with Nb-based SIS junctions. *IEEE Trans. Appl. Supercond.* **9**, 1716–1719 (1999).
- Steinhauer, S. et al. NbTiN thin films for superconducting photon detectors on photonic and two-dimensional materials. *Appl. Phys. Lett.* **116**, 171101 (2020).
- Archer, L. E. *Optical properties of ultra-thin niobium nitride films for single photon detectors*, (2017).
- Korneeva, Y. P. et al. Influence of sheet resistance and strip width on the detection efficiency saturation in micron-wide superconducting strips and large-area meanders. *Supercond. Sci. Technol.* **34**, 084001 (2021).
- Smirnov, K. et al. NbN single-photon detectors with saturated dependence of quantum efficiency. *Supercond. Sci. Technol.* **31**, 035011 (2018).
- Esmail Zadeh, I. et al. Efficient single-photon detection with 7.7 ps time resolution for photon-correlation measurements. *ACS Photonics* **7**, 1780–1787 (2020).

34. Ma, R. et al. Single photon detection performance of highly disordered NbTiN thin films. *J. Phys. Commun.* **7**, 055006 (2023).
35. China, F. et al. Highly efficient NbTiN nanostrip single-photon detectors using dielectric multilayer cavities for a 2- $\mu\text{m}$  wavelength band. *Opt. Express* **31**, 20471–20479 (2023).
36. Gantmakher, V. F. *Electrons and disorder in solids*. Vol. 130 (OUP Oxford, 2005).
37. Vetlugin, A. N., Martinelli, F., Dong, S. & Soci, C. Photon number resolution without optical mode multiplication. *Nanophotonics* **12**, 505–519 (2023).
38. Bartolf, H. et al. Current-assisted thermally activated flux liberation in ultrathin nanopatterned NbN superconducting meander structures. *Phys. Rev. B* **81**, 024502 (2010).
39. Kupryanov, M. Y. & Lukichev, V. Temperature dependence of pair-breaking current in superconductors. *Sov. J. Low Temp. Phys. (Engl. Transl.)(United States)* **6** (1980).
40. Sidorova, M., Semenov, A. D., Hübers, H.-W., Gyger, S. & Steinhauer, S. Phonon heat capacity and self-heating normal domains in NbTiN nanostrips. *Supercond. Sci. Technol.* **35**, 105005 (2022).
41. Miki, S. et al. Superconducting NbTiN nanowire single photon detectors with low kinetic inductance. *Appl. Phys. Express* **2**, 075002 (2009).
42. Shen, L., Lee, J., Hartanto, A. W., Tan, P. & Kurtsiefer, C. Wide-range wavelength-tunable photon-pair source for characterizing single-photon detectors. *Opt. Express* **29**, 3415–3424 (2021).
43. Yabuno, M., China, F., Miki, S. & Terai, H. Large-area niobium titanium nitride superconducting microstrip single-photon detector fabricated using a photolithography process. *IEEE Trans. Appl. Supercond.* **33**, 1–4 (2023).
44. ID281 Pro SNSPD System, <https://www.idquantique.com/quantum-sensing/products/id281-pro-snspd-system/>
45. Single Quantum Eos, <https://www.singlequantum.com/solutions/excellence/>
46. Scontel SSPD, <https://www.scontel.ru/sspd/>
47. You, L. et al. Superconducting nanowire single-photon detector on dielectric optical films for visible and near infrared wavelengths. *Supercond. Sci. Technol.* **30**, 084008 (2017).
48. Akhlaghi, M. K., Schelew, E. & Young, J. F. Waveguide integrated superconducting single-photon detectors implemented as near-perfect absorbers of coherent radiation. *Nat. Commun.* **6**, 8233 (2015).
49. Clem, J. R. & Berggren, K. K. Geometry-dependent critical currents in superconducting nanocircuits. *Phys. Rev. B Condens. Matter* **84**, 174510 (2011).
50. Jönsson, M. et al. Current crowding in nanoscale superconductors within the Ginzburg-Landau model. *Phys. Rev. Appl.* **17**, 064046 (2022).
51. Baghdadi, R. et al. Enhancing the performance of superconducting nanowire-based detectors with high-filling factor by using variable thickness. *Supercond. Sci. Technol.* **34**, 035010 (2021).
52. Ejrnaes, M. et al. Characterization of parallel superconducting nanowire single photon detectors. *Supercond. Sci. Technol.* **22**, 055006 (2009).
53. van der Pauw, L. J. A method of measuring the resistivity and Hall coefficient on lamellae of arbitrary shape. *Philips. Tech. Rev.* **20**, 220–224 (1958).
54. Aslamasov, L. & Larkin, A. The influence of fluctuation pairing of electrons on the conductivity of normal metal. *Phys. Lett. A* **26**, 238–239 (1968).
55. Maki, K. Critical fluctuation of the order parameter in a superconductor. I. *Prog. Theor. Phys.* **40**, 193–200 (1968).
56. Hong, C.-K., Ou, Z.-Y. & Mandel, L. Measurement of subpicosecond time intervals between two photons by interference. *Phys. Rev. Lett.* **59**, 2044 (1987).
57. Migdall, A., Polyakov, S. V., Fan, J. & Bienfang, J. C. *Single-photon generation and detection: physics and applications*. (Academic Press, 2013).

## Acknowledgements

The authors are thankful to Qi Ying Tan for her assistance with X-ray diffractometry. This research work was supported by the National Research Foundation, Singapore and A\*STAR under the Quantum Engineering Programme (QEP-P1 and NRF2021-QEP2-01-P01).

## Author contributions

C.S. and S.D. conceived the experiments, S.D. optimized NbTiN film deposition and fabricated the SNSPD devices. D.K. performed single photon measurements and SNSPD calibration. F.M. and P.B. helped with film characterization. M.P. and L.S. fabricated and calibrated the SNSPD devices during the preliminary phases of the project. A.N.V. performed absorption simulations. S.D., M.S., A.N.V., and C.S. drafted the manuscript. All authors discussed the results and reviewed the manuscript. C.K. and C.S. supervised the project.

## Competing interests

The authors declare no competing interests.

## Additional information

**Correspondence** and requests for materials should be addressed to C.S.

**Reprints and permissions information** is available at [www.nature.com/reprints](http://www.nature.com/reprints).

**Publisher's note** Springer Nature remains neutral with regard to jurisdictional claims in published maps and institutional affiliations.

**Open Access** This article is licensed under a Creative Commons Attribution-NonCommercial-NoDerivatives 4.0 International License, which permits any non-commercial use, sharing, distribution and reproduction in any medium or format, as long as you give appropriate credit to the original author(s) and the source, provide a link to the Creative Commons licence, and indicate if you modified the licensed material. You do not have permission under this licence to share adapted material derived from this article or parts of it. The images or other third party material in this article are included in the article's Creative Commons licence, unless indicated otherwise in a credit line to the material. If material is not included in the article's Creative Commons licence and your intended use is not permitted by statutory regulation or exceeds the permitted use, you will need to obtain permission directly from the copyright holder. To view a copy of this licence, visit <http://creativecommons.org/licenses/by-nc-nd/4.0/>.

© The Author(s) 2024